Ni₂C surface carbide to catalyze low-temperature graphene growth

Rafael Martinez-Gordillo,[1] Céline Varvenne,[1] Hakim Amara,[2,*] and Christophe Bichara[1]

[1]*Aix Marseille Université–CNRS, CINaM, Campus de Luminy, 13288, Marseille, France*
[2]*Laboratoire d'Etudes des Microstructures, ONERA-CNRS, Boîte Postale 72, 92322 Châtillon Cedex, France*

The possibility to grow a graphene layer using the chemical-vapor-deposition technique over a Ni₂C/Ni(111) substrate has been identified experimentally, with the advantage of having a lower processing temperature ($T <$ 500 °C), compared to standard growth over a Ni(111) surface. To understand the role of the metal carbide/metal catalyst, we first perform a static study of the Ni₂C/Ni(111) structure and of the binding and removal of a carbon atom at the surface, using both a tight-binding (TB) energetic model and *ab initio* calculations. Grand-canonical Monte Carlo TB simulations then allow us (i) to determine the thermodynamic conditions to grow graphene and (ii) to separate key reaction steps in the growth mechanism explaining how the Ni₂C/Ni(111) substrate catalyzes graphene formation at low temperature.

I. INTRODUCTION

Chemical vapor deposition (CVD) using transition- or noble-metal catalysts is currently the preferred method for high-quality graphene synthesis due to its low cost and scalability to industrial requirements [1]. In this process, a carbon-bearing molecular precursor is decomposed at the surface of a catalyst to deliver carbon and feed the growing carbon network. Using this approach, graphene synthesis has been performed successfully on a number of transition metals (such as Cu, Ir, Pt, Ni), where different mechanisms can be distinguished depending on their carbon solubility [2–4]. On metals with a low carbon solubility, carbon atoms remain at the surface after precursor decomposition and self-organize to form graphene, without significant diffusion into the bulk. When carbon solubility is larger, both carbon dissolution to the bulk and graphene formation on the surface occur, possibly followed by a surface segregation of dissolved C atoms from the bulk to the surface when the sample is cooled down. In the case of nickel, the latter mechanism is observed, where C occupies interstitial sites due to its relatively small atomic size [5–7], with a solubility limit around 3%–5%. The growth of monolayer graphene (MLG) on Ni(111) has been widely studied since this surface offers an almost perfect template for growing epitaxial graphene. Actually, the in-plane lattice constants of graphene match the surface lattice constants of Ni(111), with a lattice mismatch of only 1.3% [3]. However, the relatively high solubility of carbon in Ni and the resulting bulk reservoir effect [8–10] make graphene uniformity and control of the number of layers over large areas a very challenging task [11,12].

In the context of graphene synthesis, Ni-C compounds are known to act as both carbon source and catalyst for nucleation, suggesting that nickel carbide can be an intermediate phase for graphene formation. Typically, metastable carbide Ni₃C [13–16] has been identified in some particular conditions

to favor a solid-state graphene growth mechanism [17,18]. More interestingly, local regions with excess carbon in the form of a surface-confined nickel carbide Ni₂C have been identified in many catalytic reactions to promote the decomposition of gaseous molecules [19–21]. Unlike most other transition metals, graphene growth on Ni(111) covered by a Ni₂C surface layer [22,23] may take place and has been seen to increase the rate of graphene formation [10,21,24,25]. Furthermore, it has been shown experimentally that this surface carbide enables graphene to grow at relatively low temperatures (below 460 °C– 500 °C) [10,24,25], making this mechanism very attractive for greener graphene production. Nevertheless, most data and the corresponding literature to date were obtained by experimental observations done either after the formation of graphene [22–24] or *in situ* during the synthesis [10,21,24,25], i.e., where the atomic resolution is difficult to reach. This makes it complex to understand the atomistic mechanisms relevant to the low-temperature formation of high-quality graphene over Ni₂C.

Theory and atomistic computer simulations are ideally suited at this scale but face important difficulties due to the complexity of the synthesis methods [26]. In particular, *ab initio* calculations [24,25,27–29] are limited to short timescales and small samples. This is problematic in the present case where a theoretical study of the Ni₂C/Ni(111) substrate to grow graphene requires large supercells and finite-temperature calculations. Semiempirical (or tight-binding) [30–32] and empirical [33,34] interatomic potentials are, in principle, able to meet such requirements, but their ability to deal with the complex carbide surface structure should be carefully assessed. In the general context of carbon nanotubes and graphene growth, we developed an order-N tight-binding (TB) method to describe the Ni-C system [35]. This model was incorporated into a Monte Carlo code working in either a canonical or grand-canonical ensemble and is well suited to deal with large systems ($\sim$1000–10 000 atoms), closer to experimental conditions. This simplified TB model has been successfully applied to study graphene and carbon nanotube formation from

---

*Corresponding author: hakim.amara@onera.fr

Ni catalysts [36–38]. Recently, by combining MC simulations, *ab initio*–based calculations and *in situ* x-ray photoelectron spectroscopy, we evidenced that the interaction of epitaxial graphene with Ni(111) causes a depletion of dissolved carbon close to the surface. This should prevent additional layer formation leading to self-limiting graphene growth [12].

Here, we use both *ab initio* calculations and grand-canonical Monte Carlo (GCMC) simulations coupled to our tight-binding model to investigate the structure of the carbidic phase and its role in the graphene growth process. A careful static study of the Ni_2C/Ni(111) interface combined with the analysis of the local energy distributions reveals a heterogeneous system in which all carbon atoms in the supercell are inequivalent. The addition and removal of a single carbon atom at the surface are then investigated to characterize the surface reactivity and identify elementary steps during the first stage of the growth process. Finally, our GCMC simulations highlight thermodynamic conditions at low temperatures ($T < 700$ K) where graphene growth is observed and reveal the atomic-scale details of the low-temperature graphene formation on the reconstructed Ni surface.

II. METHOD

Our density functional theory (DFT) calculations are performed using the SIESTA code [39] in the generalized gradient approximation with the Perdew-Burke-Ernzerhof exchange-correlation functional [40]. To describe the valence electrons, double-ζ plus polarization numerical atomic orbitals are used with radii of 4.1 (5.8) bohrs for the $2s$ ($2p$) orbitals in the case of C and 7.5 (7.5) bohrs for $4s$ ($3d$) orbitals in Ni. Norm-conserving Troullier-Martin-type pseudopotentials [41] with nonlinear core correction [42] are used to represent the effect of atomic core states. To determine the occupation of electronic states, the Fermi-Dirac distribution is used with an electronic temperature of 25 meV and with a sampling of $2 \times 2 \times 1$ in k space for the supercells containing the Ni_2C/Ni(111) system, which was large enough to converge the results (a description of the structure is given in Sec. III). The charge density is represented on a real-space grid, with a mesh cutoff of 400 Ry. Structural relaxation of atomic positions was performed until the forces became lower than 0.01 eV Å^{-1}.

To describe the Ni-C system, we previously developed a model based on the TB approximation; details can be found in Ref. [35]. We use a moment (or recursion) method to determine the local electronic densities of states at a minimal (fourth moment) level, giving access to the band energy and ensuring linear scaling of the CPU time with system size. Note that in this model, van der Waals interactions were included indirectly by imposing that the model reproduce the experimental equilibrium interplane distance of a graphene layer in perfect epitaxy on Ni(111). This energy model is implemented in a Monte Carlo code in the grand-canonical ensemble (GCMC) with fixed volume, temperature T, number of metal atoms, and C chemical potential μ_C [43]. The GC algorithm used to study graphene formation consists of a series of Monte Carlo cycles. Each cycle randomly alternates displacement moves for the metal and C atoms and attempts to incorporate or remove C in a previously defined active zone (only the upper half of the box here). In addition, to obtain minimum-energy

TABLE I. Properties of fcc Ni and graphene, as computed with SIESTA and our TB model [35] and a comparison with plane-wave *ab initio* calculations [7,14,44] and experimental values [6,45,46]. ΔE_{sol}^C is the heat of solution of a C interstitial in a crystalline fcc Ni calculated according to the formula $\Delta E_{sol}^C = E_{Ni+C} - E_{Ni} - E_C$, where E_{Ni+C} is the total energy of the Ni plus interstitial C system, E_{Ni} is the total energy of Ni in the fcc structure, and E_C is the energy of the isolated C atom.

	fcc Ni						Graphene
	a_0 (Å)	B (GPa)	C' (GPa)	C_{44} (GPa)	M_0 (μ_B/at)	ΔE_{sol}^C (eV)	a_{Gr} (Å)
SIESTA	3.52	266	66	147	0.58	0.82	2.46
Plane waves	3.52	202	64	135	0.62	0.70	2.47
Tight binding	3.52	182	69	97		0.45	2.47
Expt.	3.52	188	55	132	0.61	0.43	

structures with the TB model in conditions comparable to static structural relaxations performed in DFT, MC simulations were performed at 1 K, with only displacement moves.

To validate these different atomic interaction models, it is worth comparing their results to available experimental data and plane-wave calculations for some simple properties. Table I displays the lattice parameters of fcc Ni and graphene, elastic constants, and magnetic moment for fcc Ni. Lattice parameters are well predicted by all interaction models. The Ni bulk modulus is well reproduced by the TB model but overestimated in SIESTA calculations: this is due to the optimized localized basis set, which was constrained to be small here. The experimental shear elastic moduli C' and C_{44} are reproduced within 25% by the TB model, and the agreement is improved in SIESTA calculations, which are also closer to the plane-wave values. Finally, the magnetic moment of Ni obtained with SIESTA is very close to the plane-wave result and to the experimental value. At this level, both interaction models thus appear reasonable for the description of the Ni/C system. In addition, we note that the TB model has been applied previously in many different situations involving a large variety of Ni-C interactions [12,36–38]. In all cases the model was fairly accurate when compared to experiments and/or to *ab initio* calculations. Typical error bars are of the order of 0.1–1 eV, which should be compared to total energies of the order of 5–10 eV (C-C bond: 7 eV, Ni-Ni bond: 4.5 eV, and Ni-C bond: 5 eV). This is obviously not negligible, but it should be kept in mind that *ab initio* methods can also show rather large dispersions, mainly in the case of point or localized defects where atomic relaxations can be important [47]. For the sake of completeness, additional TB and DFT comparisons will be performed in this study for the Ni_2C/Ni(111) system.

III. STRUCTURAL STUDY OF THE Ni_2C/Ni(111) INTERFACE

In this section, we perform a detailed study of the zero-temperature structure of the Ni_2C/Ni(111) interface. In-depth calculations are performed with the lighter TB energetic model and are compared with DFT calculations for some specific cases. This study allows us to identify the most stable interface
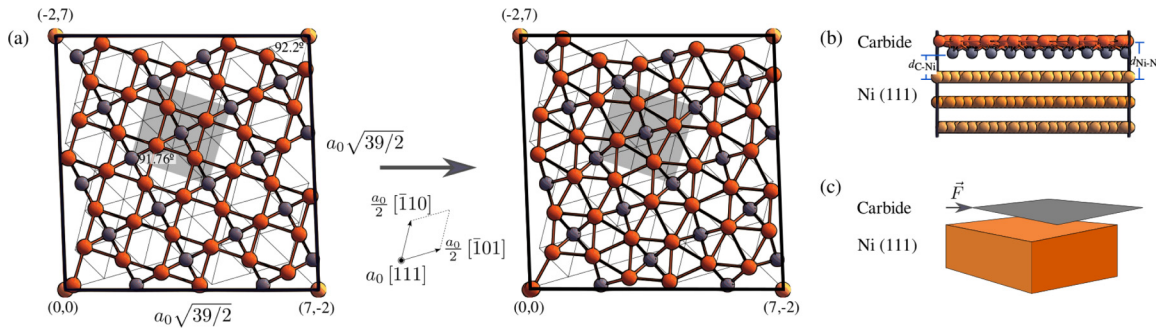
FIG. 1. Atomic structure of the Ni$_2$C/Ni(111) system. (a) Supercell view in the (111) plane, with the carbide layer before and after the clock reconstruction. The thin lines indicate the underlying fcc Ni lattice in the (111) plane. The supercell periodicity vectors are given in units of the in-plane fcc Ni basis vectors $a_0/2[\bar{1}01]$ and $a_0/2[\bar{1}10]$. The shaded zone highlights the in-plane unit cell of the Ni$_2$C carbide. (b) Side view of the system showing the carbide layer and the three (111) planes of fcc Ni. (c) Scheme representing the shift vector $\vec{F}$ of the Ni$_2$C layer with respect to the Ni(111) substrate which is applied to study the stability of the system (see text).

structure and also provides insights into the mechanical stability of the surface carbide on the Ni(111) substrate.

A. Technical details

The surface carbide has been identified experimentally [20,23,48] and displays a reconstruction of the outermost layer of the Ni(111) surface, called "clock" reconstruction, where the topmost Ni atoms move around C atoms by alternating clockwise and counterclockwise rotations. This distortion preserves the shape of the carbon squares, while the squares of nickel atoms not surrounding the C atoms become rhombi. Similar clock reconstructions of (100) surfaces in fcc Ni and other fcc metals have been well characterized, both experimentally and theoretically [28,49]. The final Ni$_2$C/Ni(111) structure then corresponds to a larger supercell made from a coincidence lattice of both systems [22,50]. To study the Ni$_2$C/Ni(111) system, calculations are performed with a supercell built as follows. First, a fcc Ni slab is constructed in a [111] orientation, with three Ni layers (45 Ni atoms). The coincident supercell within the (111) plane is shown in Fig. 1(a) and produces an almost square supercell in the (111) plane. A carbide layer Ni$_2$C of 40 Ni and 20 C atoms, with the clock reconstruction described in Fig. 1(a), is then added on top of one of the Ni(111) free surfaces [see Fig. 1(b)]. Periodic boundary conditions are applied, and to avoid spurious interactions, a vacuum space of ∼20 Å is included between open surfaces. When relaxing this system in atomistic simulations, the Ni atoms of the bottom free surface are kept fixed to their fcc bulk positions.

In order to determine the stablest position for the carbide layer, relative to the Ni(111) slab, we apply the following method using the TB model. As indicated in Fig. 1(c), we compute the adhesion energy of the carbide layer for different shift vectors $\vec{F}$ applied to it. In these calculations, atoms are allowed to relax only in the [111] direction of the fcc Ni, i.e., perpendicular to the carbide layer. Such a strategy is common in the context of a generalized stacking fault energy map computation in solids [51,52], and we apply it here to the metal carbide/metal interface. The adhesion energy is defined as

$$E_{\text{adh}} = \frac{1}{A}(E_{\text{Ni}_2\text{C/Ni(111)}} - E_{\text{Ni}_2\text{C}} - E_{\text{Ni(111)}}), \qquad (1)$$

where $E_{\text{Ni}_2\text{C/Ni(111)}}$ is the energy of the Ni$_2$C/Ni(111) system, $E_{\text{Ni}_2\text{C}}$ is the energy of the freestanding carbide layer, $E_{\text{Ni(111)}}$ is the energy of the Ni(111) slab, and A is the area of the supercell in the (111) plane. Adhesion energies are calculated on a regular 12×12 grid of $\vec{F}$ vectors within the Ni $(a_0/2[\bar{1}01], a_0/2[\bar{1}10])$ unit cell, which then contains all the necessary information, and then interpolated to obtain a continuous adhesion energy map. The TB model easily deals with such a thin grid, which would have been more challenging for *ab initio* simulations.

B. Energy landscape of the interface

The adhesion energy map resulting from the above procedure is shown in Fig. 2(a). This energy landscape has mirror symmetries with respect to the $(\bar{2}11)$ and $(0\bar{1}1)$ planes and is compatible with the lattice vectors of both the Ni(111) and Ni$_2$C structures in the (111) plane. Along the $[\bar{2}11]$ direction, important variations of energies are seen, and the partially relaxed potential-energy landscape is made of two similar alternating plateau maxima and minima regions. In contrast, the potential energy is essentially invariant along the $[0\bar{1}1]$ direction. This suggests the existence of a low-friction direction upon shearing for the Ni$_2$C layer with respect to the Ni(111) substrate.

The relaxation is, however, incomplete in the previous procedure, as the in-plane degrees of freedom were frozen. To better elucidate the different possible stable states for the structure of the Ni$_2$C/Ni(111) system, we thus perform a full relaxation on selected structures [see dots for the selected glide vectors $\vec{F}$ in Fig. 2(b)], allowing the system to fully relax in all three coordinates. The displacement of the Ni$_2$C carbide layer relative to the Ni(111) slab is monitored during the relaxation process. For the systems starting in the minima region, the net carbide layer displacement is not significant, and they all remain in the minimum valley [see Fig. 2(c), group A], with an adhesion energy of -4.37 ± 0.028 J m^{-2}. For systems with initial shift vectors located in a maxima region, all configurations fall into a second minimum valley (group B) that was not identified by the previous procedure. The net carbide displacement is also not significant for this group of structures, which has an adhesion energy of -4.13 ± 0.031 J m^{-2}, thus higher than that of group A. Finally, to further check the

(a)

(b)

(c)

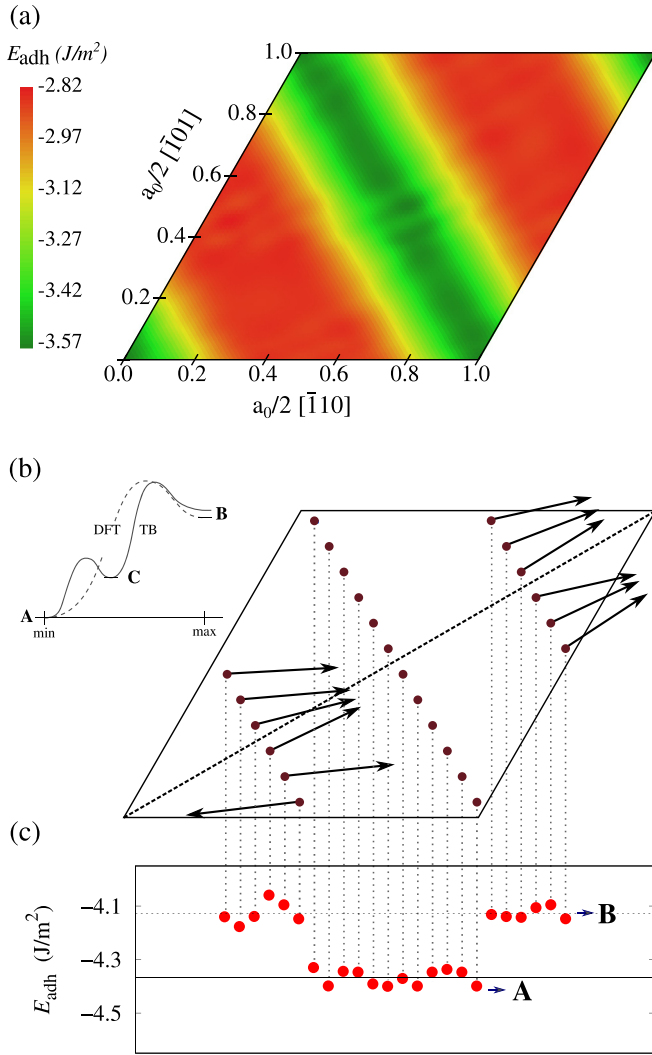FIG. 2. Relative stability of the Ni$_2$C layer on the Ni(111) substrate, with the TB model. (a) Map of adhesion energies, as computed with Eq. (1), for all possible shift vectors $\vec{F}$ and with atomic relaxations performed only along the Ni [111] direction. (b) Scheme showing the $\vec{F}$ vectors of the specific configurations of the Ni$_2$C/Ni(111) that are then fully relaxed. The arrows indicate the in-plane displacement experienced by the Ni$_2$C layer relative to the Ni(111) substrate during a subsequent annealing of the structures (see text). The inset illustrates the aspect of the energy landscape along the [$\bar{2}$11] direction for TB and DFT. (c) Fully relaxed adhesion energies for these selected configurations.

energy landscape of the interface, we perform a $T = 350$ K annealing of the group-A and -B configurations. The group-A ones stay at their in-plane position, while the group-B ones fall into an intermediate family of minima [see the arrows in Fig. 2(b), and the C label in the inset]. After this process, the group-A configurations remains the lowest in energy. The energy landscape, as described by the TB model, is thus invariant along the [0$\bar{1}$1] direction and is composed of three groups of degenerate minima.

We now compare the TB results with DFT calculations for two specific glide vectors $\vec{F}$: one within group A and one within group B. Both group-A and -B structures are energy minima

and stay at their in-plane initial positions in DFT, as with TB for the same initial positions [see the schematic view in the inset in Fig. 2(b)]. With DFT, the group-A and -B configurations have adhesion energies of -3.83 and -3.60 J m^{-2}, respectively. As with TB, the group-A structures are stabler than group B, and the energy difference between the two families is $\sim$0.23 J m^{-2} ($\sim$0.25 J m^{-2} with TB), i.e., of the order of the stacking fault energy. This energy difference is therefore very similar within both interaction models. Considering the structural details of the group-A configurations, after relaxation, both with DFT and TB, C atoms are located between the Ni atoms of the carbide and the topmost layer of Ni(111). The distances of C atoms to the substrate ($d_{\text{C-Ni}}$ in Fig. 1) differ for each C position within the supercell, being 1.68 ± 0.26 Å for DFT and 1.58 ± 0.17 Å for TB, thus having large standard deviations within both interaction models. The distance between Ni atoms from the substrate to Ni atoms from the carbide ($d_{\text{Ni-Ni}}$ in Fig. 1) is 2.18 ± 0.1 Å for DFT and 2.24 ± 0.1 Å for TB, thus very similar in both models and again with rather important variations. Finally, local energies of C atoms in the carbide layer show important differences, as large as 0.7 eV with both interaction models.

To conclude, this study allows us to identify the stablest structures for the interface Ni$_2$C/Ni(111): it actually consists of a degenerate family of configurations, corresponding to the group-A structures. The flatness of the potential-energy landscape along the [0$\bar{1}$1] direction suggests a low friction/easy glide direction for the carbide on the Ni(111) substrate. The comparison between TB and DFT calculations shows that the TB model provides a very reasonable description of the Ni$_2$C/Ni(111) system, which is structurally very far from the compounds and structures initially used for developing the TB model [35]. This good transferability of our TB approach supports its use for graphene growth studies that cannot be performed with DFT.

IV. ELEMENTARY STEPS FOR GRAPHENE FORMATION

In this section, we use static relaxations to investigate some of the elementary steps that are possibly involved during graphene growth on the Ni$_2$C/Ni(111) system.

A. Carbon addition

In order to investigate the ability of the Ni$_2$C/Ni(111) system to capture C atoms at its surface, thus acting as starting point for growing graphene, we compute the interaction energy of a single C atom with the Ni$_2$C/Ni(111) surface as

$$E_{\text{int}} = E_{\text{C+Ni}_2\text{C/Ni(111)}} - E_{\text{Ni}_2\text{C/Ni(111)}} - E_{\text{C}}, \qquad (2)$$

with $E_{\text{C+Ni}_2\text{C/Ni(111)}}$ is the energy of the system with one added C atom and the Ni$_2$C/Ni(111) substrate, $E_{\text{Ni}_2\text{C/Ni}}(111)$ is the energy of the Ni$_2$C/Ni(111) substrate, and E_{C} is the energy of the isolated C atom (which vanishes with the TB model). A negative E_{int} then corresponds to an attractive interaction.

Technically, a lot of possible positions exist for the C addition at the surface. An inkling of the need for a detailed investigation is given by the inequivalency of the C atoms within the carbide layer, as identified previously. Their different local structural environments and different local energies suggest a
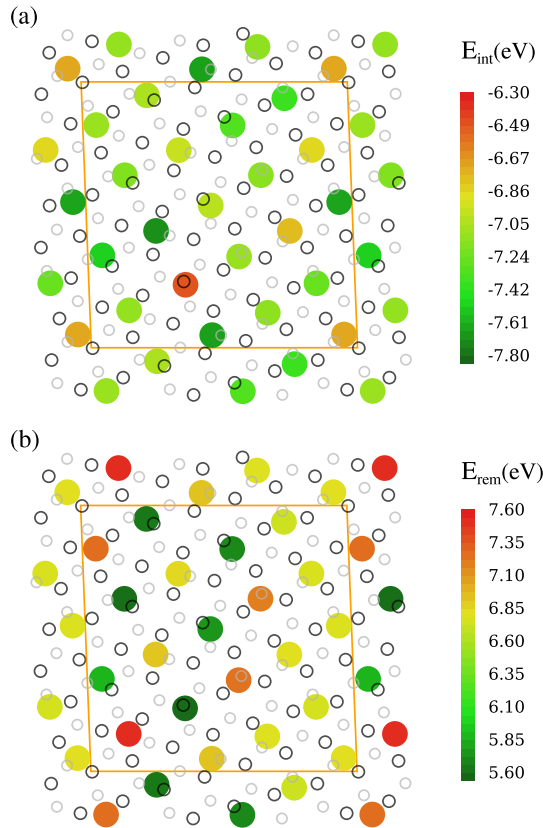
(a)

(b)

FIG. 3. Maps representing (a) the interaction energies [Eq. (2)] of a single C atom forming a C dimer with the Ni$_2$C/Ni(111) system and (b) the energy cost to remove a C atom from the carbide layer [Eq. (2)]. Energies are computed for all C atom positions in the Ni$_2$C layer within the supercell, adopting the following representation: big dots correspond to C atoms from Ni$_2$C and are colored according to the appropriate energy value, and open circles represent two successive (111) layers of fcc Ni. Atomic positions are from the relaxed initial group-A configuration before adding or removing carbon. The Ni atoms from the carbide are omitted for clarity.

variation of reactivity across different addition sites within the supercell. A series of calculations is thus performed with TB. In these calculations, we start from the stablest Ni$_2$C/Ni(111) substrate configuration (group A). A single C atom is then added to the surface of the system, located exactly on top of one of the C atoms from the carbide, and the system is relaxed. The resulting interaction energies, computed through Eq. (2), are given in Fig. 3(a). Interactions are all significantly attractive, showing the ability of the carbide to chemisorb individual C atoms. Variations across different addition positions are large, 1.22 eV, with the most attractive positions corresponding to the formation of C-C dimers on top of fcc-like or hcp-like positions of the Ni(111) slab.

Now comparing TB results with DFT calculations for some specific positions for the C addition, we consider two of the surface positions forming dimers with C atoms from Ni$_2$C, which have local hcp-like and fcc-like environments with respect to the Ni(111) slab, respectively. We also consider a surface position with the added C having three nearest-neighbor Ni atoms (denoted as the "no-dimer" configuration) and two fcc

TABLE II. Interaction energy E_{int} (in eV) of a single C atom with the Ni$_2$C/Ni(111) system [see Eq. (2)] for different carbon positions, using both TB and DFT calculations.

| Position | Type | | E_{int} (eV) | | Config. |
			SIESTA	TB	
Surface	dimer FCC	□	−6.11	−7.07	
	dimer HCP	□	−6.12	−7.06	
	no dimer	△	−5.68	−4.00	
Bulk	O site below C		−6.59	−7.37	
	O site not below C		−6.76	−7.43	

Ni octahedral (O) insertion sites, one below a C atom from the carbide and the other below Ni atoms from the carbide. The interaction energies for these different configurations are shown in Table II. Within both models, all interaction energies are attractive; equivalent E_{int} values are found for the two surface dimer configurations, and comparable values are found for the two bulk configurations. The relative stabilities of the different configurations for the single C atom added to the Ni$_2$C/Ni(111) system calculated using our TB model and DFT are in good agreement and rank as follows : bulk positions > dimer positions ≫ no-dimer configuration. We note that the difference between TB and DFT energies is larger for the no-dimer situation but in any case is less attractive than the other configurations. Consequently, in the GCMC simulations of graphene formation on the carbidic phase that explore situations not too far from the thermodynamic equilibrium, these no-dimer configurations will be less visited than the surface dimer ones. We will come back to this point in Sec. V.

The present set of calculations therefore (i) suggests that C atoms forming the Ni$_2$C carbide can actually act as nucleation centers for graphene growth and (ii) confirms that the energetic and structural descriptions provided by our TB Hamiltonian are accurate enough to describe the Ni$_2$C/Ni(111) system.

B. Carbon removal

We now investigate the ability of the Ni$_2$C layer to act as a source of carbon for graphene formation, using TB static relaxations. As before, due to the inequivalency of C atoms in the relaxed and most stable Ni$_2$C/Ni(111) system, we compute the energy cost of removing one C atom from the carbide for all the C atoms within the supercell (starting from the same group-A configuration as before). This energy is defined as

$$E_{rem} = E_{(Ni_2C-C)/Ni(111)} - E_{Ni_2C/Ni(111)} + E_C, \qquad (3)$$

where $E_{(Ni_2C-C)/Ni(111)}$ is the energy of the relaxed system with one removed C atom, $E_{Ni_2C/Ni}$ is the energy of the relaxed Ni$_2$C/Ni(111) system, and E_C is the energy of the isolated C atom.

Figure 3(b) gives the resulting E_{rem} values, which are all positive, meaning that removing C atoms from the carbide to infinity is not favorable. In the actual graphene growth process, however, the removed C atom would be included in a graphene layer. Therefore, to discuss the ability of Ni$_2$C to act as a carbon source for graphene formation, the reference energy
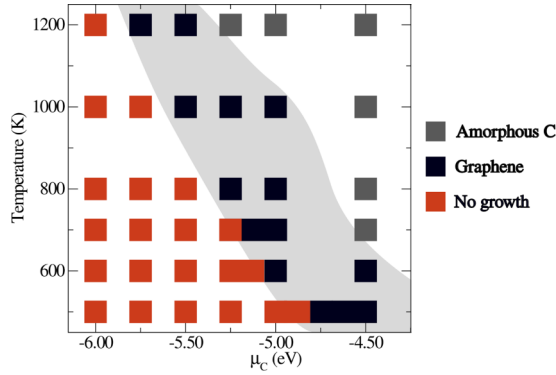
FIG. 4. Identification of the thermodynamic conditions (T, μ_c) to stabilize a graphene layer over the Ni$_2$C/Ni(111) system. When going to the top right corner of the graphene zone, i.e., close to the domain of amorphous carbon, the obtained graphene layer contains more defects.

for the carbon atom in E_{rem} should be the cohesive energy of a graphene monolayer, which is $\sim$7.5 eV with the TB model. With this shift, the range of energies becomes mostly negative, suggesting the carbon removal and incorporation into graphene are possible. Important variations in E_{rem} (of $\sim$1.9 eV) are seen across different C atomic sites, and thus, only some specific carbon atoms from the carbide should be possible to include in the graphene layer. For the sake of comparison, we performed a few DFT calculations of E_{rem} for five specific carbon atoms from the Ni$_2$C layer. The obtained values are 8.0 ± 0.12 eV, which are thus higher and less scattered than the TB results. While incomplete, this set of DFT calculations suggests that the role of the Ni$_2$C layer as a carbon source for graphene formation might be overestimated by the TB model, and this will be further discussed in Sec. V.

V. GRAPHENE FORMATION ON Ni$_2$C/Ni(111)

We now study how graphene growth mechanisms are influenced by the Ni$_2$C surface. To this aim, we perform GCMC simulations to examine the self-organization of carbon atoms on Ni$_2$C/Ni(111). More precisely, our goal is to determine the thermodynamic conditions (μ_C, T) for graphene formation, as the thermochemical conditions of the precursor decomposition reaction in CVD lead to the presence of carbon atoms close to the surface of the catalyst at a given chemical potential μ_C [53]. In this context, MC simulations in the grand-canonical ensemble are perfectly adapted to address this issue. Such GCMC simulations are performed on a supercell that is twice as large as the previous one, thus having 390 atoms in total in the initial configuration and up to 700–800 atoms during the GCMC process.

Figure 4 presents the final equilibrium states obtained on Ni$_2$C/Ni(111) at temperatures ranging from 500 to 1200 K, summarizing the outcomes of GCMC simulations across different values of μ_C (−6.00 to −4.50 eV/atom). For low values of μ_C, single C atoms are adsorbed, possibly forming small linear chains but no rings. This corresponds to a domain where no graphene growth is observed. When the chemical potential increases, more carbon atoms are added to the system, leading to the growth of a graphenelike layer where a majority of C
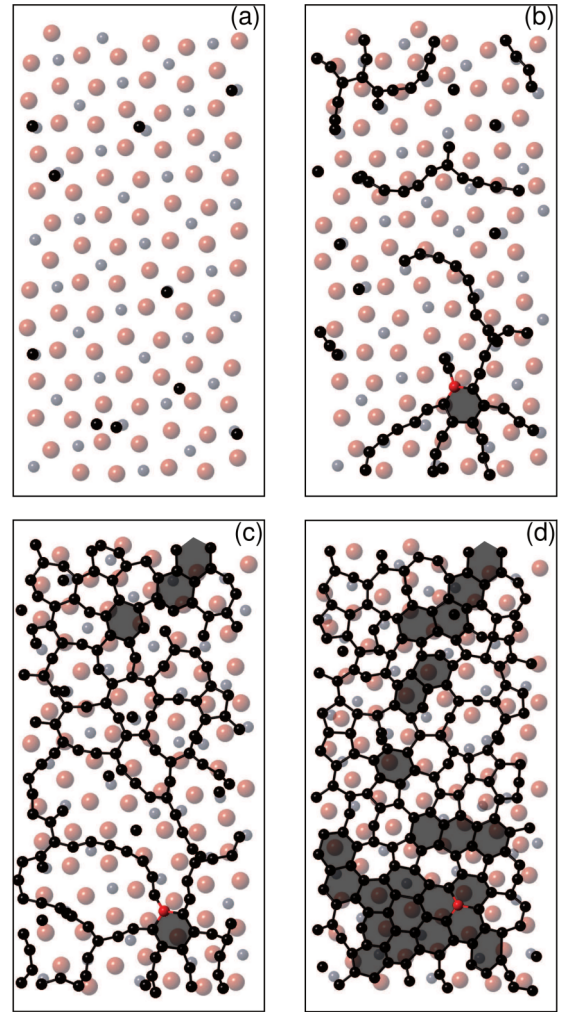

FIG. 5. Snapshots of atomic configurations during the growth of graphene on a Ni$_2$C/Ni(111) interface at 500 K and $\mu_C = -4.75$ eV/atom. Ni atoms are orange, C atoms of Ni$_2$C are gray, and outer C atoms on the surface to form graphene are black. The Ni atoms from Ni(111) are omitted for clarity. (a) Atoms adsorbed on top of C atoms of Ni$_2$C. (b) C atoms of the interface (in red) integrated into the graphene network. (c) Chains forming and crossing to form hexagons. (d) Equilibrium structures at 500 K.

atoms are threefold coordinated. At higher μ_C, the number of stable carbon atoms outside the carbidic surface is important and corresponds to a three-dimensional amorphous C phase. More interestingly, μ_C values are identified where graphene growth is observed at low temperatures ($T < 700$ K), in agreement with experimental observations [10,21,24,25]. In the case of pristine Ni(111), previous GCMC simulations [12] have highlighted that graphene formation is expected only at temperatures higher than 800 K for comparable μ_C values. This supports the key role played by the carbide in lowering the growth temperature.

Important steps at the atomic scale in graphene formation on Ni$_2$C/Ni(111) are visualized in snapshots taken at different stages obtained by GCMC calculations at 500 K and $\mu_C = -4.75$ eV/atom (see Fig. 5). In these thermodynamic conditions, a sp^2 layer containing numerous hexagonal rings

is formed. During the first steps of the simulation, most of the C atoms are adsorbed on the surface and form C-C dimers [see Fig. 5(a)], as discussed in the previous section. Consequently, the first steps of graphene formation can be observed at low temperature since, in contrast to Ni(111), C atoms present in the surface-confined nickel carbide Ni$_2$C enhance the surface reactivity by trapping C atoms close to the surface. Then, C atoms form short chains on the surface that eventually cross-link with each other to form carbon rings that act as nucleation centers to grow a monolayer graphene structure [see Figs. 5(b) and 5(c)]. Such a mechanism has already been observed in the case of graphene growth on Ni(111) [32,36]. Interestingly, some C atoms of the carbide layer can also be integrated into the graphene network, in agreement with the two-layer mechanism proposed in [10] (typically 1–3 C atoms from the 40 C atoms of the carbide layer). The GCMC simulations of graphene formation on the carbidic phase therefore reveal the two elementary mechanisms that were postulated and investigated by static simulations in Secs. IV A and IV B. Both assist the nucleation and growth of graphene at a relatively low temperature. However, we mentioned earlier that some differences exist between the TB and DFT interaction and removal energies describing these two elementary mechanisms. Consequently, the TB-GCMC simulations likely underestimate the C adsorption on no-dimer positions and overestimate the quantity of carbon atoms from Ni$_2$C included in the monolayer graphene. A precise quantification of the statistical weight of the different mechanisms versus temperature and μ_C for each of the interaction models would require the development of a simplified statistical physics model for this process, which is beyond the scope of the present work.

As seen in Fig. 5(d), the final configurations are plagued by a high concentration of atomic-scale defects, e.g., heptagon-pentagon topological defects. This is partly caused by the lower sampling efficiency of our Monte Carlo algorithm at lower temperature. Such defects can be healed by increasing the temperature, with the help of the metal catalyst [54,55]. This tendency is further confirmed by calculations done at 700 K, where the number of hexagonal rings is significantly larger [see Fig. 6(a)]. Furthermore, C-C bonds between the MLG and the interface are clearly present [see Fig. 6(b), where a side view is presented], leading to the buckling of the carbon structure. Such bonds are formed during the first steps of the nucleation process where C atoms are adsorbed on the surface to form C-C dimers [see Fig. 5(a)]. As a result, these anchor points tend to keep the MLG fixed, thus hindering subsequent rotation of graphene with respect to the Ni(111) surface. Such defects should heal over longer timescales, but their presence could explain the absence of rotated graphene reported using *in situ* scanning tunneling microscopy and x-ray photoelectron spectroscopy [10].

VI. CONCLUSION

In summary, we have presented DFT calculations and tight-binding Monte Carlo simulations to investigate the role of the Ni$_2$C carbidic phase in low-temperature graphene growth. In the first step, the structure and stability of the Ni$_2$C/Ni(111) interface were identified via the determination of its energy
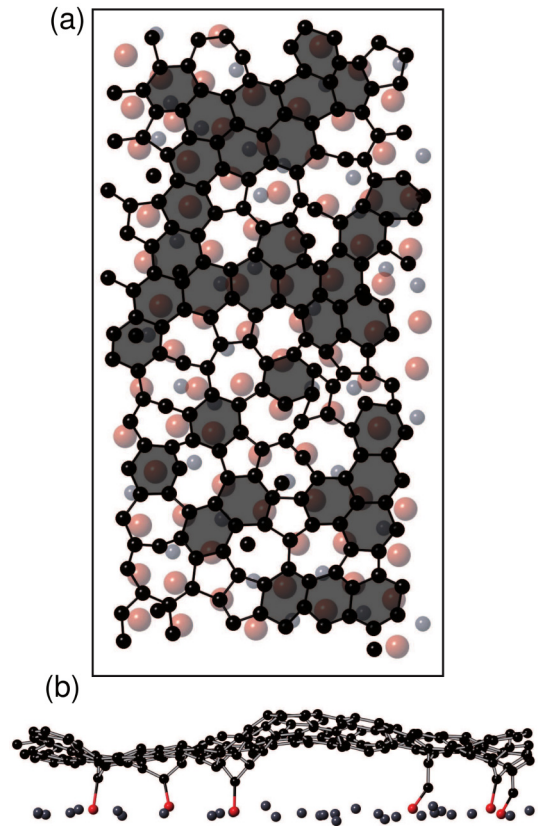

FIG. 6. Equilibrium structures at 700 K, obtained from GCMC simulations performed on a Ni$_2$C/Ni(111) interface for $\mu_C = -5.15$ eV/atom. Ni atoms are orange, C atoms of Ni$_2$C are gray, and outer C atoms on the surface to form graphene are black. The Ni atoms from Ni(111) are omitted for clarity. (a) Top view, where many hexagons can be seen. (b) Side view, where C-C bonds between graphene and the interface (C atoms are in red) are clearly present.

landscape, and its reactivity with respect to the carbon species was analyzed. By performing GCMC simulations, we have found thermodynamic conditions to grow graphene at relatively low temperature. The presence of C atoms from the Ni$_2$C carbide acting as nucleation centers for graphene growth and the inclusion of C atoms from Ni$_2$C in the MLG were determined as key factors promoting graphene formation at low temperature. Moreover, the attachment of graphene to the interface via C-C bonds should limit its rotation with respect to the Ni(111) substrate. All the results presented here are highly relevant for controlled graphene growth and in agreement with experimental data. To go further, other growth modes suggested in the experimental literature have to be investigated [10,21,24,25], in particular, the in-plane conversion mechanism where graphene grows alongside Ni$_2$C and the conventional graphene growth over Ni(111) with Ni$_2$C appearing only after the synthesis as a result of bulk-dissolved C precipitation. In this context, the clock reconstruction of the Ni(111) surface to form Ni$_2$C in the presence of C atoms implies the removal of Ni atoms, unless steps and edges help, as shown experimentally and theoretically [23,56]. This would require extending our GCMC algorithm to include attempts to remove existing Ni atoms. Such approaches are currently under development to undertake appropriate large-scale simulations.

[1] S. Hofmann, P. Braeuninger-Weimer, and R. S. Weatherup, J. Phys. Chem. Lett. **6**, 2714 (2015).

[2] J. Wintterlin and M. L. Bocquet, Surf. Sci. **603**, 1841 (2009).

[3] M. Batzill, Surf. Sci. Rep. **67**, 83 (2012).

[4] A. Cabrero-Vilatela, R. S. Weatherup, P. Braeuninger-Weimer, S. Caneva, and S. Hofmann, Nanoscale **8**, 2149 (2016).

[5] A. Cottrell, *Chemical Bonding in Transition Metal Carbides* (Institute of Materials, London, 1995).

[6] D. J. Siegel and J. Hamilton, Phys. Rev. B **68**, 094105 (2003).

[7] X. Hu, T. Björkman, H. Lipsanen, L. Sun, and A. V. Krasheninnikov, J. Phys. Chem. Lett. **6**, 3263 (2015).

[8] A. Reina, X. Jia, J. Ho, D. Nezich, H. Son, V. Bulovic, M. S. Dresselhaus, and J. Kong, Nano Lett. **9**, 30 (2009).

[9] R. Addou, A. Dahal, P. Sutter, and M. Batzill, Appl. Phys. Lett. **100**, 021601 (2012).

[10] L. L. Patera, C. Africh, R. S. Weatherup, R. Blume, S. Bhardwaj, C. Castellarin-Cudia, A. Knop-Gericke, R. Schloegl, G. Comelli, S. Hofmann, and C. Cepek, ACS Nano **7**, 7901 (2013).

[11] R. S. Weatherup, B. C. Bayer, R. Blume, C. Baehtz, P. R. Kidambi, M. Fouquet, C. T. Wirth, R. Schlögl, and S. Hofmann, Chem. Phys. Chem. **13**, 2544 (2012).

[12] R. S. Weatherup, H. Amara, R. Blume, B. Dlubak, B. C. Bayer, M. Diarra, M. Bahri, A. Cabrero-Vilatela, S. Caneva, P. R. Kidambi, M.-B. Martin, C. Deranlot, P. Seneor, R. Schloegl, F. Ducastelle, C. Bichara, and S. Hofmann, J. Am. Chem. Soc. **136**, 13698 (2014).

[13] I. R. Shein, N. I. Medvedeva, and A. L. Ivanovskii, Phys. B **371**, 126 (2006).

[14] C. M. Fang, M. H. F. Sluiter, M. A. van Huis, and H. W. Zandbergen, Phys. Rev. B **86**, 134114 (2012).

[15] L. Yue, R. Sabiryanov, E. M. Kirkpatrick, and D. L. Leslie-Pelecky, Phys. Rev. B **62**, 8969 (2000).

[16] V. K. Portnoi, A. V. Leonov, S. N. Mudretsova, and S. A. Fedotov, Phys. Met. Metallogr. **109**, 153 (2010).

[17] M. Jiao, K. Li, W. Guan, Y. Wang, Z. Wu, A. J. Page, and K. Morokuma, Sci. Rep. **5**, 12091 (2015).

[18] W. Xiong, Y. S. Zhou, W. J. Hou, T. Guillemet, J. F. Silvain, Y. Gao, M. Lahaye, E. Lebraud, S. Xu, X. W. Wang, D. A. Cullen, K. L. More, L. Jiang, and Y. F. Lu, RSC Adv. **5**, 99037 (2015).

[19] D. E. Gardin, J. D. Batteas, M. A. V. Hove, and G. A. Somorjai, Surf. Sci. **296**, 25 (1993).

[20] H. Nakano, J. Ogawa, and J. Nakamura, Surf. Sci. **514**, 256 (2002).

[21] M. Wei, Q. Fu, Y. Yang, W. Wei, E. Crumlin, H. Bluhm, and X. Bao, J. Phys. Chem. C **119**, 13590 (2015).

[22] J. J. McCarroll, T. Edmonds, and R. C. Pitkethly, Nature (London) **223**, 1260 (1969).

[23] C. Klink, I. Stensgaard, F. Besenbacher, and E. Lagsgaard, Surf. Sci. **342**, 250 (1995).

[24] J. Lahiri, T. Miller, L. Adamska, I. Oleynik, and M. Batzill, Nano Lett. **11**, 518 (2010).

[25] P. Jacobson, B. Stöger, A. Garhofer, G. S. Parkinson, M. Schmid, R. Caudillo, F. Mittendorfer, J. Redinger, and U. Diebold, ACS Nano **6**, 3564 (2012).

[26] A. J. Page, F. Ding, S. Irle, and K. Morokuma, Rep. Prog. Phys. **78**, 036501 (2015).

[27] Y. Shibuta, R. Arifin, K. Shimamura, T. Oguri, F. Shimojo, and S. Yamaguchi, Chem. Phys. Lett. **565**, 92 (2013).

[28] A. Nandula, Q. T. Trinh, M. Saeys, and A. N. Alexandrova, Angew. Chem., Int. Ed. **54**, 5312 (2015).

[29] R. Arifin, Y. Shibuta, K. Shimamura, and F. Shimojo, Eur. Phys. J. B **88**, 303 (2015).

[30] H.-B. Li, A. J. Page, Y. Wang, S. Irle, and K. Morokuma, Chem. Commun. **48**, 7937 (2012).

[31] J. A. Elliott, Y. Shibuta, H. Amara, C. Bichara, and E. C. Neyts, Nanoscale **5**, 6662 (2013).

[32] A. J. Page, I. Mitchell, H.-B. Li, Y. Wang, M.-g. Jiao, S. Irle, and K. Morokuma, J. Phys. Chem. C **120**, 13851 (2016).

[33] E. C. Neyts, A. C. van Duin, and A. Bogaerts, Nanoscale **5**, 7250 (2013).

[34] Y. Lu and X. Yang, Carbon **81**, 564 (2015).

[35] H. Amara, J.-M. Roussel, C. Bichara, J.-P. Gaspard, and F. Ducastelle, Phys. Rev. B **79**, 014109 (2009).

[36] H. Amara, C. Bichara, and F. Ducastelle, Phys. Rev. B **73**, 113404 (2006).

[37] H. Amara, C. Bichara, and F. Ducastelle, Phys. Rev. Lett. **100**, 056105 (2008).

[38] M. Diarra, A. Zappelli, H. Amara, F. Ducastelle, and C. Bichara, Phys. Rev. Lett. **109**, 185501 (2012).

[39] J. M. Soler, E. Artacho, J. D. Gale, A. García, J. Junquera, P. Ordejón, and D. Sánchez-Portal, J. Phys.: Condens. Matter **14**, 2745 (2002).

[40] J. P. Perdew, K. Burke, and M. Ernzerhof, Phys. Rev. Lett. **77**, 3865 (1996).

[41] N. Troullier and J. L. Martins, Phys. Rev. B **43**, 1993 (1991).

[42] S. G. Louie, S. Froyen, and M. L. Cohen, Phys. Rev. B **26**, 1738 (1982).

[43] D. Frenkel and B. Smith, *Understanding Molecular Simulation* (Academic, London, 2002).

[44] A. Metsue, A. Oudriss, and X. Feaugas, Philos. Mag. **94**, 3978 (2014).

[45] C. Kittel, *Introduction to Solid State Physics*, 6th ed. (Wiley, New York, 1986).

[46] G. A. Alers, J. R. Neighbours, and H. Sato, J. Phys. Chem. Sol. **13**, 40 (1960).

[47] E. Clouet, C. Varvenne, and T. Jourdan, Comput. Mater. Sci. **147**, 49 (2018).

[48] J. Nakamura, H. Hirano, M. Xie, I. Matsuo, T. Yamada, and K.-i. Tanaka, Surf. Sci. **222**, L809 (1989).

[49] J. Shelton, H. Patil, and J. Blakely, Surf. Sci. **43**, 493 (1974).

[50] K. Hermann, J. Phys.: Condens. Matter **24**, 314210 (2012).

[51] V. V. Bulatov and W. Cai, *Computer Simulations of Dislocations*, edited by A. P. Sutton and R. E. Rudd, Oxford Series on Materials Modeling (Oxford University Press, Oxford, 2006).

[52] C. Varvenne, O. Mackain, and E. Clouet, Acta Mater. **78**, 65 (2014).

[53] J. Snoeck, J. Catal. **169**, 240 (1997).

[54] Q. Yuan, Z. Xu, B. I. Yakobson, and F. Ding, Phys. Rev. Lett. **108**, 245505 (2012).

[55] M. Diarra, H. Amara, C. Bichara, and F. Ducastelle, Phys. Rev. B **85**, 245446 (2012).

[56] R. Vang, J. Honkala, S. Dahl, E. Vestergaard, J. Schnadt, B. Clausen, J. Nørskov, and F. Besenbacher, Surf. Sci. **600**, 66 (2006).